

# Synergistic Doping and Surface Decoration of Carbon Nitride Macrostructures by Single Crystal Design

Jesús Barrio, Shmuel Barzilai,\* Neeta Karjule, Pilar Amo-Ochoa, Félix Zamora, and Menny Shalom\*



Cite This: *ACS Appl. Energy Mater.* 2021, 4, 1868–1875



Read Online

ACCESS |



Metrics & More



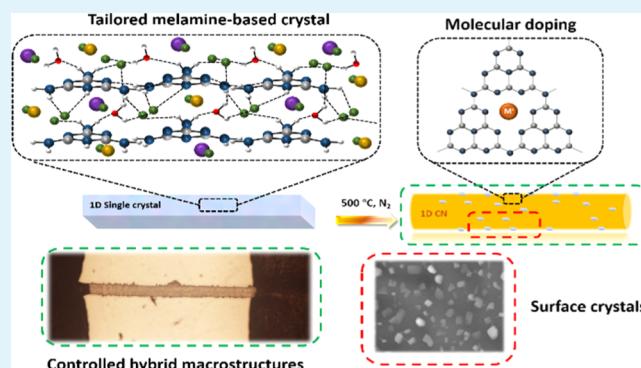
Article Recommendations



Supporting Information

**ABSTRACT:** Tailored design of hybrid carbon nitride (CN) materials is quite challenging because of the drawbacks of the solid-state reaction, and the utilization of single crystals containing C–N monomers as reactants for the high-temperature reaction has been proven to imprint a given chemical composition, morphology, or electronic structure. We report the one-pot synthesis of alkali-containing CN macrostructures with ionic crystals on its surface by utilizing a tailored melamine–hydrochloride-based molecular single crystal containing NaCl and KCl as reactants. Structural and optical investigations reveal that upon calcination, molecular doping with Na<sup>+</sup> and K<sup>+</sup> is achieved, and additionally, the ionic species remain on the surface of the materials, resulting in an enhanced H<sub>2</sub> evolution performance through water splitting owing to a high ionic strength of the reaction media. Additionally, the most stable configuration of the alkaline metals in the CN lattice is evaluated by DFT calculations. This work provides an approach for the rational design of CN and other related metal-free materials with controllable properties for energy-related applications and devices.

**KEYWORDS:** carbon nitride, photocatalysis, doping, crystal design, hydrogen evolution, alkali metals doped carbon nitride



## 1. INTRODUCTION

Graphitic carbon nitride (CN) materials have attracted widespread attention as metal-free semiconductors for a wide variety of energy-related applications, covering photo-electrochemistry for water splitting,<sup>1–4</sup> CO<sub>2</sub> reduction,<sup>5–7</sup> and organic transformations.<sup>8</sup> Recently, tailored design of properties such as the electronic band structure or the surface composition has allowed the use of CN materials in other fields, such as sensing,<sup>9–11</sup> polymer chemistry,<sup>12</sup> and optoelectronic devices.<sup>13,14</sup> The introduction of alkali metals and their ionic salts has been proven to augment the photocatalytic activity of these materials by virtue of the ability of metals such as Li, Na, or K to finely tune the band structure of CN.<sup>15,16</sup> Furthermore, Maschmeyer and co-workers have recently shown that the ionic strength of the reaction media strongly affects the photocatalytic activity in CN-based systems modified with alkali metals, owing to a dielectric screening effect.<sup>17</sup> Recently, we and others showed the possibility of designing the structural, thermal, and photophysical properties of CN (with or without heteroatoms) by using melamine-based single crystals as reactants.<sup>18–24</sup> Upon calcination, the high crystalline stability of the monomers allows them to retain their order at high temperatures. In this work, we show the synthesis of novel alkali metal-containing melamine crystals and their utilization for the high-temperature synthesis of CN polymers. Upon thermal condensation, molecular doping is

achieved, which enhances the photocatalytic performance in the hydrogen evolution reaction (HER) through water splitting. Additionally, the CN surface is decorated with salt crystals. Using this innovative method, together with theoretical calculations, enabled us to elucidate the role of the alkali metals embedded within the CN framework, distinct from those in the solution.

## 2. EXPERIMENTAL SECTION

**2.1. Synthesis of Melamine-Based Crystals and CN Materials.** Melaminium chloride hemihydrate crystals were prepared by slow evaporation of a 50 mL solution containing melamine (150 mg, 1.2 mmol) and HCl in water (37%, 2% v/v). Metal-doped crystals were prepared following the same approach, dissolving melamine (150 mg, 1.2 mmol) along with a given alkali metal salt, either NaCl (70.1 mg, 1.2 mmol) or KCl (89.5 mg, 1.2 mmol) in a 1:1 molar ratio. A 1:0.5:0.5 molar ratio was employed to prepare the crystal containing both salts (150 mg, 1.2 mmol for melamine, 35 mg, 0.6 mmol for NaCl, and 45 mg, 0.6 mmol for KCl). Graphitic CN

Received: November 26, 2020

Accepted: January 7, 2021

Published: January 19, 2021



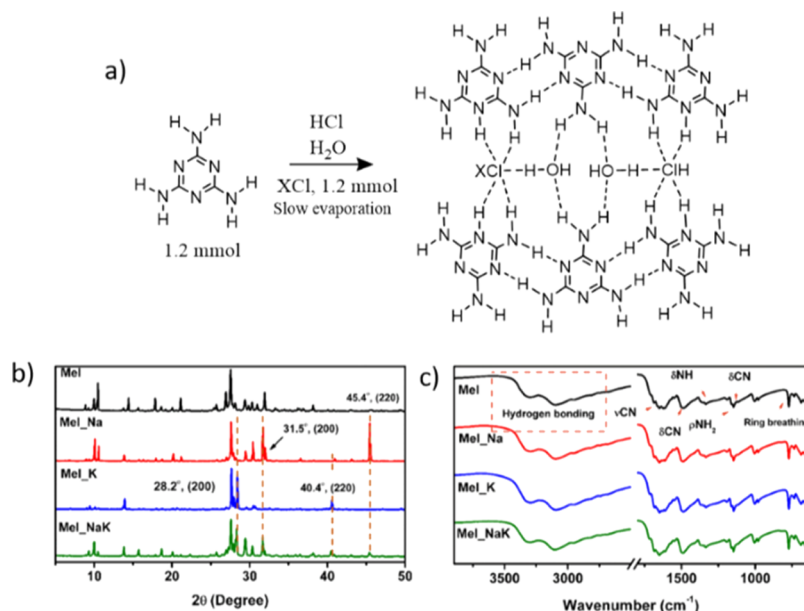


**Figure 1.** Proposed structure of M- (X = Na or K) crystals (a); XRD patterns (b) and FTIR spectra (c) of the prepared crystals.

materials were prepared by thermal condensation of the prepared crystals at 500 °C for 4 h under a N<sub>2</sub> atmosphere.

**2.2. Photocatalytic Hydrogen Production.** The measurements were carried out at a constant temperature of 25 °C under an inert Ar atmosphere. For this, 15 mg of the photocatalyst was placed in a 50 mL Schlenk flask in a solution (19 mL) containing water and triethanolamine (TEOA) in a 9:1 (v/v) ratio and 19.6 μL of H<sub>2</sub>PtCl<sub>6</sub> solution (8% in water). The mixture was kept under a constant Ar flow for 30 min before the reaction was started by switching on a −100 W white LED array (Bridge lux BXRA-50CS300; λ > 410 nm), following a similar methodology previously reported by our group.<sup>25</sup> The amount of evolved gas in the headspace was evaluated by gas chromatography (Agilent 7820 GC system), by injecting 0.5 mL, after having performed a calibration line with known amounts of H<sub>2</sub>. The average quantum yield (AQY) was obtained utilizing LEDs (Thorlabs, Model no. M40SL4 and M430L4) equipped with a 405 nm bandpass filter and an average intensity of 35 mW cm<sup>−2</sup>. AQY measurements were carried out in a sealed reactor connected to an argon line and an Agilent 7820 GC system with a total solution volume of 8 mL, having the same proportions as the measurements performed in the Schlenk flask. The reactor was continuously purged with argon in darkness in order to remove the existing gases, and the purging process was monitored by automatic sampling every 11 min. After purging, the LED was switched on, the amount of hydrogen gas produced was recorded, and the integrated area was used for the calculation of the AQY according to the formula:  $AQY = N_e/N_p \times 100\% = 2 M/N_p \times 100\%$ , where  $N_e$  is the number of reaction electrons,  $N_p$  is the number of incident photons, and  $M$  is the number of H<sub>2</sub> molecules.<sup>26</sup>

**2.3. Electrochemical Measurements.** Electrochemical measurements were recorded using a three-electrode system on an Autolab potentiostat (Metrohm, PGSTAT 101). A Pt foil electrode and an Ag/AgCl (3 M KCl) electrode were used as the counter and reference electrodes, respectively. Mott–Schottky (1/C<sup>2</sup> vs V) measurements were carried out at a frequency of 1, 2, 2.48, 3.2 kHz in 1 M Na<sub>2</sub>SO<sub>4</sub> aqueous solution as the electrolyte. Nyquist plots of the samples were measured in the frequency range from 100 kHz to 10 mHz at an applied voltage of 1.23 V versus RHE.

**2.4. DFT Calculations.** Density functional theory (DFT) was utilized to compute the interaction between sodium and potassium and CN surfaces. We considered a supercell with one layer of CN, arranged in a tri-*s*-triazine geometry containing 24 carbon atoms, 32 nitrogen atoms, and a top vacuum layer. The initial slab was relaxed to define the optimum lattice parameter and to allow the atoms in the slab to adjust their relaxed positions. The calculations were carried out

using the Quantum-ESPRESSO package<sup>27</sup> and performed on a periodically repeated supercell. To define the preferred location of the sodium and potassium cations over the CN surface and to compute the adsorption energies, all atoms in the supercell were allowed to relax, and the electronic properties were then computed. The adsorption energy ( $E_{ads}$ ) of each alkali metal was computed according to the following equation

$$E_{ads} = E_{rlx}^{sys} - \left( E_{rlx}^{CN} + \sum_i^n E^{K \text{ or Na}} \right)$$

where  $E_{rlx}^{sys}$  is the total energy of each system after relaxation,  $E_{rlx}^{CN}$  is the relaxed energy of the CN surface,  $E^{K \text{ or Na}}$  is the energy of an isolated alkali metal cation, and  $n$  is the number of such cations on the surface, computed for a selected coverage area. The ion core was described by plane wave (PAW) pseudopotentials,<sup>28</sup> and the valence electrons (2s, 2p electrons for C and N atoms, 2s 2p 3s electrons for Na, and 3s 3p 4s electrons for K atoms) were treated explicitly with a kinetic cutoff of 50 Ry for the wave function and 350 Ry for the charge density. The exchange–correlation potential was treated within the Perdew–Burke–Ernzerhof generalized gradient approximation,<sup>29</sup> and a  $k$ -mesh of  $2 \times 2 \times 1$  was constructed according to the Monkhorst and Pack scheme.<sup>30</sup> The relaxations were carried out until the change in energy was less than  $5 \times 10^{-5}$  Ry, and the residual forces of all atoms were less than  $10^{-3}$  Ry/B.<sup>3</sup> For the final relaxed structures, a self-consistent convergence criterion of  $10^{-6}$  Ry was imposed. Identical conditions and convergence criteria were employed for all systems.

**2.5. Characterization.** Scanning electron microscopy (SEM) images of the CN materials were obtained with a JEOL JSM-7400 microscope and a field emission gun source operating at 3.5 kV. The porosity was calculated by the Brunauer–Emmett–Teller approach from nitrogen-sorption measurements performed on a Quantachrome Novatouch NT LX<sup>3</sup> system. Fourier transform infrared (FTIR) spectroscopy was performed with a Thermo Scientific Nicolet iN10Mx infrared microscope. Fluorescence measurements were carried out in an Edinburgh instrument, FLS920P fluorimeter. UV–vis absorption spectra were obtained with a Cary 100 spectrophotometer. X-ray photoelectron spectroscopy (XPS) was performed with a Thermo Fisher Scientific ESCALAB 250 spectrometer using monochromatic K $\alpha$  X-rays (1456.6 eV). X-ray diffraction (XRD) patterns were measured with a PANalytical Empyrean diffractometer using Cu K $\alpha$  radiation. Magic-angle spinning (MAS) NMR experiments were carried out on a Bruker AVANCE III 500 MHz narrow-bore spectrometer, using a 4 mm double-resonance MAS

**Scheme 1.** Scheme of the Preparation of CN Materials, with Both Alkali Metal Salt Crystals at the Surface and Molecular Doping, from a Melamine-Based Crystal

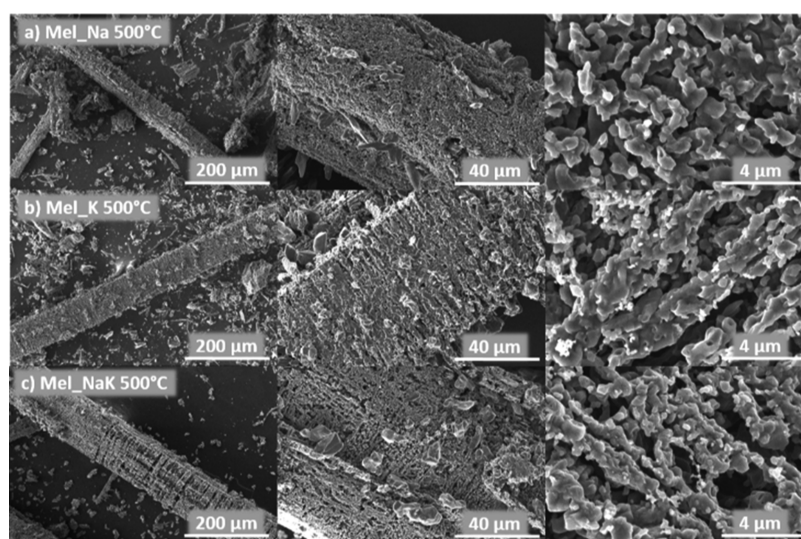
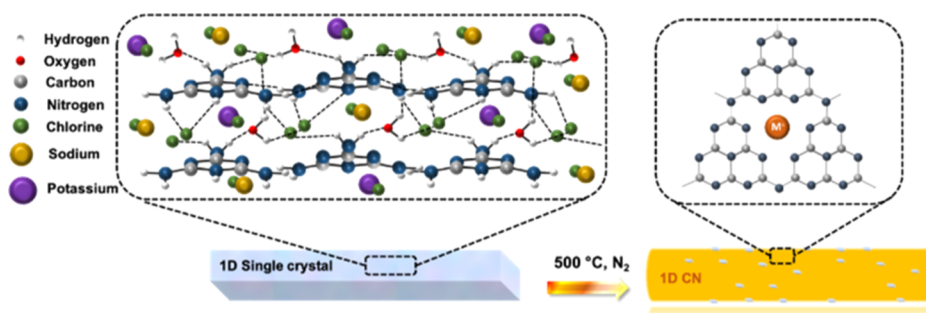


**Figure 2.** SEM Images of CN materials prepared with (a) NaCl, (b) KCl, and (c) both salts.

probe at a spinning rate of 8 KHz.  $^{13}\text{C}$  cross-polarization (CP) MAS experiments were carried out using a  $2.5\ \mu\text{s}$   $^1\text{H}$   $90^\circ$  pulse, a 2 ms mixing time, and a 3 s recycle delay between acquisitions.  $^1\text{H}$  direct excitation experiments were carried out using a  $2.5\ \mu\text{s}$   $90^\circ$  pulse and a 2 s recycle delay. Electrical conductivity measurements were performed by the two-contact method: individual CN macrostructures were contacted with graphite ink between two Tungsten tips, and a sweeping voltage between  $-10$  and  $+10$  V was applied at room temperature. Electric current values were collected, and a curve  $I/V$  was obtained along with the physical parameters of the CN macrostructures and Ohm's Law ( $V = IR$ ), where  $I$  (A) is the intensity and  $R$  ( $\Omega$ ) is the resistance. The resistivity depends on the geometric parameters of the sample  $\rho = R(S/L)$ , where  $S$  is the transversal section of the sample and  $L$  is the distance between the two contact points. Those values were obtained by comparison with an atomic force microscopy cantilever of length  $200\ \mu\text{m}$ . The values of the electrical conductivity ( $\sigma$ ) were then calculated, with  $\sigma = \rho^{-1}$ .

### 3. RESULTS AND DISCUSSION

Melaminium chloride hemihydrate single crystals were grown by slow evaporation of a solution of melamine in water containing 2% (v/v) HCl (37%).<sup>18,31,32</sup> Alkali metal-containing crystals (Mel-Na, Mel-K, and Mel-NaK) were prepared in the same fashion, introducing an alkali metal salt (NaCl and KCl) in a 1:1 melamine/salt molar ratio or in a 1:0.5:0.5 melamine/NaCl/KCl molar ratio where two salts were used (Figure 1a).<sup>33,34</sup> The modification of the crystal structure of the melamine crystals is supported by XRD patterns. XRD measurements reveal emerging peaks corre-

sponding to the (220) NaCl crystal plane at  $31.5$  and  $45.4^\circ$  and to the KCl (200) and (220) crystal planes at  $28.2$  and at  $40.4^\circ$ , respectively (Figure 1b).<sup>35,36</sup> Furthermore, FTIR spectroscopy confirms the establishment of a hydrogen-bonded supramolecular assembly (Figure 1c). The molecular structure of the prepared crystals was determined by single-crystal XRD. The structures obtained correspond in all cases to melaminium chloride hemihydrate, as previously reported by our research group and others<sup>18,31,37</sup> and did not show the inclusion of either of the cations, therefore suggesting that the salts were located on the surface of the melamine-based crystal or impregnated within the pore (Scheme 1).

Thermal condensation of the prepared crystals at  $500\ ^\circ\text{C}$  under  $\text{N}_2$  atmosphere yields CN microstructures with the length in the millimeter range and the width in the order of a hundred of micrometers, as shown by SEM images (Figure 2). The resulting materials were subjected to thermogravimetric analysis (TGA, Figure S1). The weight difference at  $500\ ^\circ\text{C}$  between the CN material with and without salts implies that approximately 12–13% of the original weight is due to the salts within the CN structure.

The FTIR spectra confirm the formation of a polymeric CN adduct with residual cyano groups, a result of the polymerization in the presence of  $\text{Na}^+$  and  $\text{K}^+$  ion species.<sup>38</sup> The XRD patterns show peaks of remaining starting salts, implying the presence of small salt crystals on the surface of the CN materials (Scheme 1, Figure S2). This was further confirmed by high-resolution SEM coupled with energy-dispersive X-ray



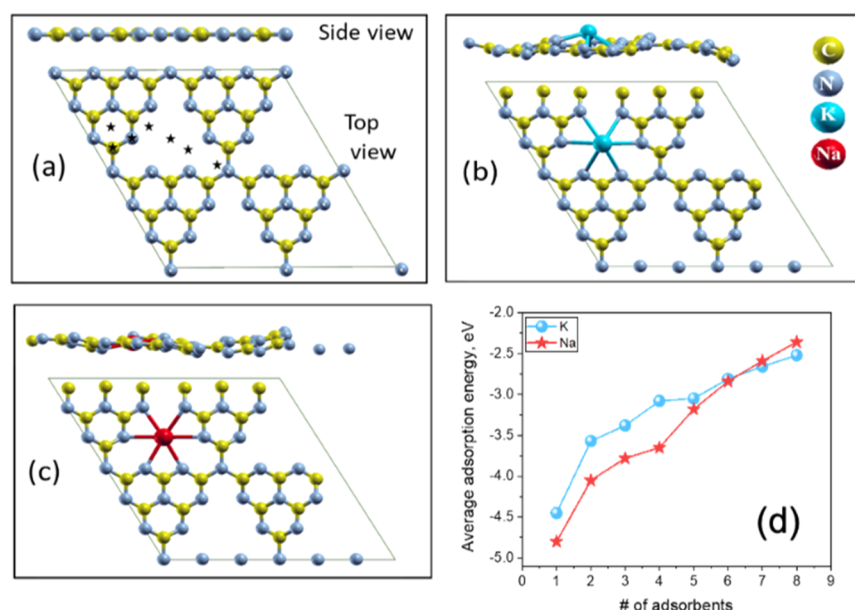


**Figure 3.** Side and top views of the relaxed CN structure without adsorbed alkali metal cations; the black stars represent the initial position of the sodium and potassium cations utilized for the relaxation (a), with the favored position for potassium (b) and sodium (c). Average adsorption energy of  $K^+$  and  $Na^+$  on the CN surface for various number of cations in the computed coverage area (d).

spectroscopy, which shows the presence of micrometric crystals on the surface of Mel–NaK (Figure S3, S4). The analysis of the photophysical properties of the materials by UV–vis and fluorescence spectroscopy discloses a narrowing of the band gap down to 2.65 eV for Mel–NaK (vs 2.75 eV for the reference CN) corresponding to an absorption edge at around 490 nm (Figure S5). Additionally, the fluorescence intensity of the materials is substantially quenched upon the addition of alkali metal salts, implying nonradiative pathways of the photoexcited charge recombination and an indication of the presence of additional surface states (Figure S6).<sup>39,40</sup>

XPS shows the common chemical states for C 1s and N 1s of CN materials. The presence of both Na and K was confirmed. The  $Na^+$  concentrations calculated from Na 1s were 1 and 2 at. % (at. % = atomic percent) for Mel–Na and Mel–NaK, respectively. The  $K^+$  concentrations calculated from K 2p were 4 and 5 at. % for Mel–K and Mel–NaK, respectively (Table S1). Nevertheless, no chemical contributions for Cl 2p<sup>3</sup> were observed, indicating molecular doping with the cations solely (Figures S7–S9). Additionally, we observed that upon doping with both  $Na^+$  and  $K^+$ , the binding energies corresponding to the chemical states of C 1s and N 1s were shifted to lower values (Table S2), suggesting an interaction between the alkali metal ions and the CN lattice.<sup>41</sup> The materials were further analyzed by solid-state NMR. The  $^1H$  MAS NMR spectrum showed two signals with peak maxima at  $\sim 9.4$  and  $\sim 4.3$  ppm, attributable to the presence of  $-NH_x$  groups and residual water in the heptazine lattices, respectively (Figure S10a).<sup>42</sup>  $^1H$  MAS NMR studies indicate the presence of melon-like NH-bridged heptazine-based structures with some  $-NH$  and  $-NH_2$  terminations. The  $^{13}C$  CP MAS NMR spectrum showed two clear signals. A signal corresponding to the C atoms bonded to  $-NH_2$  groups ( $N_2C-NH_2$ ) was observed at 164.24 ppm, whereas the characteristic peak of  $sp^2$  C–N bonds appeared at 155.79 ppm ( $CN_3$ ), showing the formation of tri-s-triazine or heptazine moieties (Figure S10b).<sup>43</sup>

In order to elucidate the binding modes of the alkali metal ions within the CN lattice, DFT simulations were carried out. For that, sodium and potassium cations were initially placed on the CN surface at seven different locations (Figure 3a), and the adsorption energy of each alkali element was computed after relaxation. During the relaxation, both the sodium and potassium cations leave their initial positions (see “\*” mark in Figure 3a) and move toward the heptazine pore or “nitrogen cavity” while decreasing the total energy of each system. This location was found to be the only stable adsorption site. Figure 3b,c shows the preferred adsorption site for potassium and sodium, respectively. The top view shows that both alkali elements found their relaxed site centered in the nitrogen pots. However, the side view unveils that the potassium cation is located out of the CN plane and the sodium cation, a smaller ion, preferred to be embedded within the plane.

The adsorption energy of each alkali element is rather high and decreases with increasing adsorbent surface concentration. As can be seen in Figure 3d, for up to four adsorbents, the Na cations are more energetically attractive, but at higher concentrations, the adsorption of potassium cations becomes favorable. This trend is related to the preferred position of each element. Figure S11 shows the adsorption configurations of Na and K cations on the CN surface at given concentrations. The preferred adsorption site of Na is embedded in the nitrogen pots of the CN. This location remains favorable up to full coverage, which is attained at four Na cations in our surface model (Figure S11a, b). For higher concentrations, the Na cations leave their relaxed location, so that two cations may occupy the same nitrogen pot: they are directed out of the plane on the opposite sides of the CN surface, with a concomitant increase in the Na–N bond length (Figure S11c). This new configuration decreases the excess adsorption energies (the additional increment of the total adsorption energy) of the cations. However, this situation is different for K cations since their preferred site is not embedded within the CN plane and, therefore, only a small change in their equilibrium bond length is observed when two cations occupy

the same nitrogen pot (Figure S11d–f). Thus, for a mixture of Na and K atoms, we expect that for a small concentration, up to  $\approx 6$  at. %, which is equivalent to four adsorbents in our surface model, Na will primarily occupy the adsorption sites, whereas at higher concentration, where the number of cations surpasses the number of sites, potassium will dominate these sites. Figure 4 illustrates this preference for high coverage area,

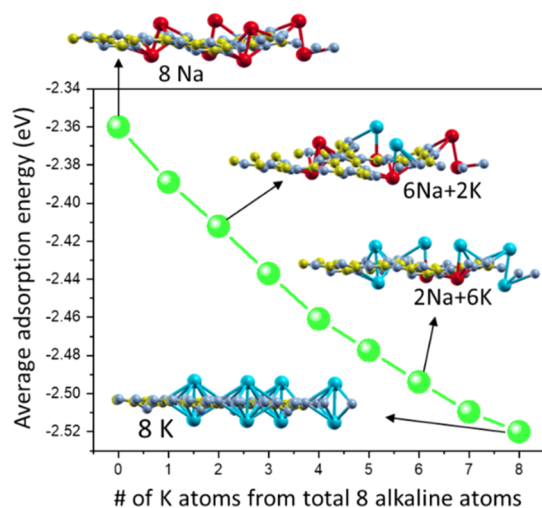


**Figure 4.** Average adsorption energy of eight mixed alkali metal cations on CN.

namely, for eight alkali metal cations (12.5 at. %) on the CN surface; the adsorption energy of eight potassium cations is energetically preferred relative to other configurations, which include sodium atoms.

Upon washing with distilled water overnight, the salt crystals on the CN surface were completely removed, as proven by the

XRD patterns (Scheme S1, Figure S12); an estimation of the salt/CN composition was obtained by weighing the material sample before and after washing (Table S3). XPS measurements confirmed the presence of both Na and K in the washed materials, with concentrations within 1 to 3 at. % (Figures S13, S14 Table S4), which proves the molecular doping of the CN frameworks. Additionally, the photophysical properties are lightly altered after washing; the absorption band edges are slightly blue-shifted (Figure 5a,b). The band structure of the materials after washing was determined using Mott–Schottky measurements and Tauc plots. From this analysis, we could observe a minor variation in the conduction and valence band positions in all doped semiconductors, which can potentially favor their performance in photocatalytic applications (Figure 5c–d, Figure S15).

The prepared materials were utilized as photocatalysts for the HER,<sup>44,45</sup> which was carried out in a water/TEOA (9:1 v/v) solution with Pt (3 wt %) as a cocatalyst. We want to note that in the absence of Pt, no  $\text{H}_2$  was produced. All doped materials showed enhanced photocatalytic performance compared to the reference material. Particularly, the one containing both Na and K (Mel–NaK) reached the high value of  $270 \mu\text{mol H}_2 \text{ h}^{-1} \text{ g}^{-1}$  before washing (Figure 6a), which corresponds to a 9.8% AQY under illumination at 405 nm. To the best of our knowledge, this is one of the highest reported AQY values for CN materials derived from self-assembled supramolecular structures, crystals, and cocrystals (Table S5, Figure 6c). After washing the surface salt, the materials follow the same trend with slightly lower values, which suggest that the presence of ionic salts in the media and close to the CN photocatalyst (as the surface salt crystals begin to slowly dissolve) augments the performance by a dielectric screening effect.<sup>17</sup> Nevertheless, the washed sample M–NaK still showed an AQY of 5.4% with higher stability than the unwashed counterpart (Figure 6d), indicating that the decrease in

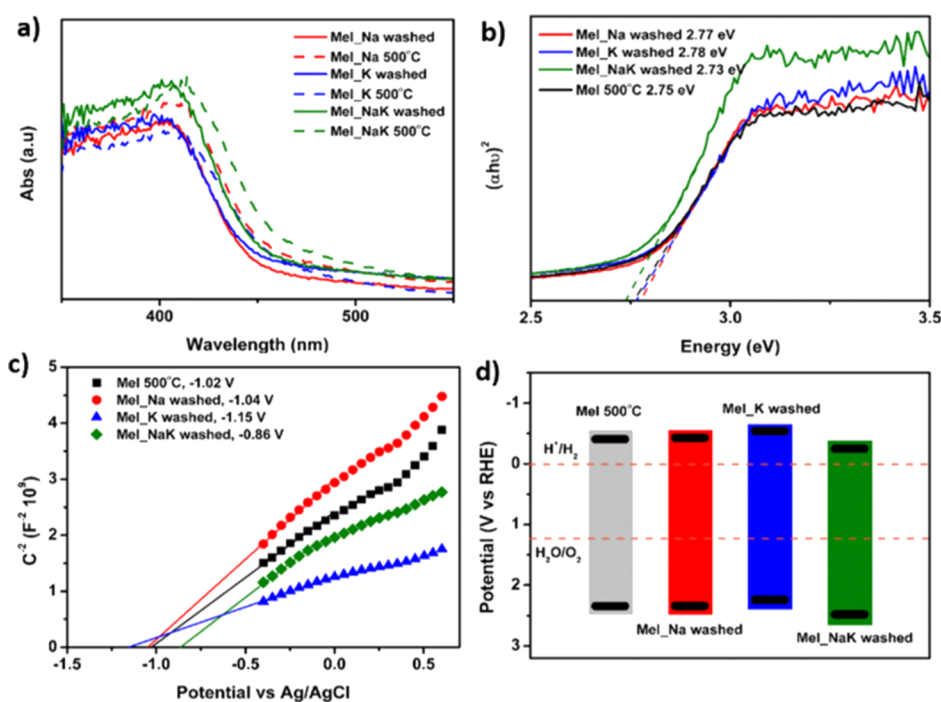


**Figure 5.** UV/vis spectra (a) and Tau plot (b) of the CN materials. Mott–Schottky measurements (c) and calculated band structure (d) of CN materials.

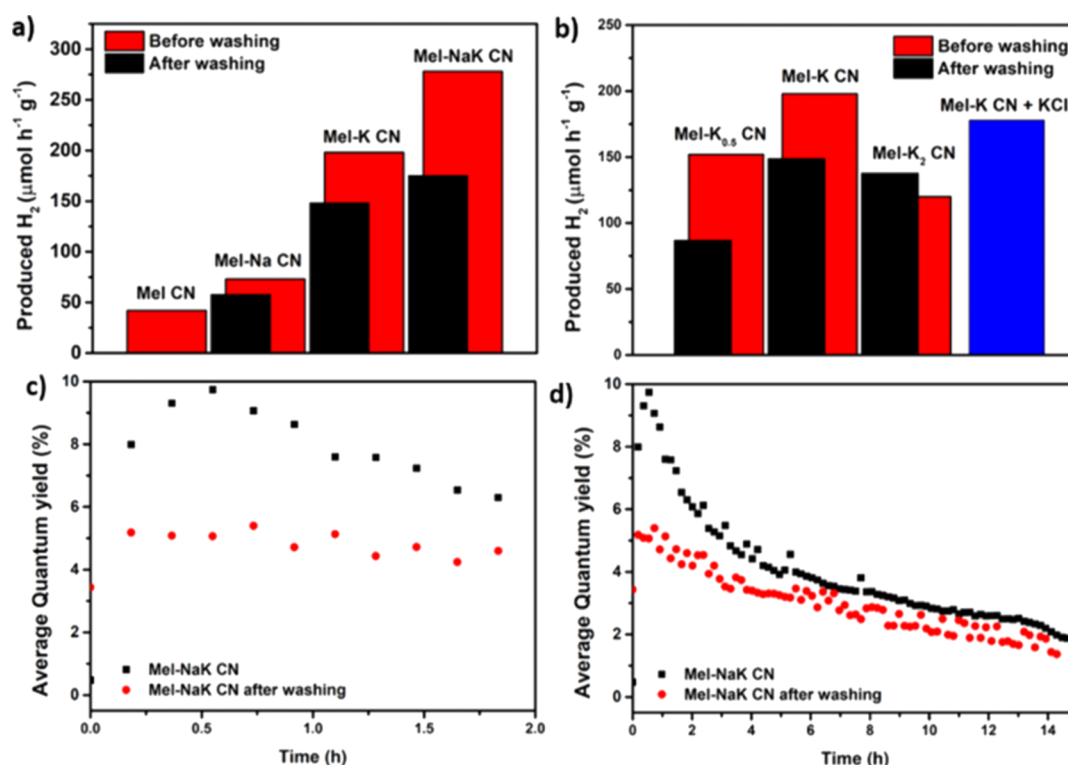


**Figure 6.**  $H_2$  production values of CN materials with various doping concentrations (a) and various amounts of potassium salt (b), AQY measurements (c), and stability test in quantum yield measurements (d).

performance for the unwashed sample is mainly due to a lowering of the ionic strength near the surface of the CN photocatalyst as the concentration of salt near the CN surface gradually equilibrates with that of the whole solution. In order to investigate the influence of the amount of metal in the initial crystal, we prepared melamine–KCl crystals with different molar ratios, namely, 1:0.5 and 1:2. XRD patterns confirmed the presence of KCl in both crystals (Figure S16a) and in the corresponding CN materials (Figure S16b). Interestingly, XPS suggested that the molecular doping does not increase with increasing KCl amounts utilized in the synthesis, indicating that a larger amount of salt was present as crystals on the surface of the macrostructures (Figure S17, Table S6, S7). Nevertheless, both the materials (derived from Mel- $K_{0.5}$  and Mel- $K_2$ ) showed lower performance than Mel-KCN (Figure 6b). To further show the good stability of the Mel-NaK CN photocatalyst, its structure and morphology after HER were characterized. The XRD pattern (Figure S18) shows that there are no changes in the graphitic structure of CN and that all diffraction peaks corresponding to surface salts vanish except from the (220) peak of KCl at  $40.4^\circ$ . SEM images suggest certain changes in the morphology of Mel-NaK CN (Figure S19). TEM images show the presence of thin CN layers containing Pt NPs of  $16.1 \pm 2.6$  nm, which are formed by photodeposition in the initial stage of the photocatalytic measurements (Figure S20, S21). Finally, we wanted to corroborate the positive effect on the photocatalytic activity of the increase in the ionic strength of the reaction media, which is induced by the presence of alkali metal salts. We measured the photocatalytic activity of washed Mel-K CN in a reaction media supplemented with an amount of KCl determined from the data obtained above (see Table S3): we observed that the photocatalytic activity rose to a value that is almost as high as

that of the unwashed sample, indicating that the salts at the surface of the material increase the ionic strength of the media and hence the photocatalytic performance, thanks to a dielectric screening effect (Figure 6b).

We additionally studied the linear sweep voltammetry with and without illumination of the most active material under a wide potential range, as illustrated in Figure S22. Noticeably, the obtained photocurrent densities are improved gradually along with the applied bias, and a remarkable difference can be observed with the reference CN in both dark conditions and under illumination. Electrochemical impedance spectroscopy (Figure S22b) suggests that introducing Na and K atoms into the CN can facilitate the charge separation.

In order to address the origin of the photocatalytic activity, we measured the porosity and conductivity of the materials. All surface area values were very low ( $3\text{--}6 \text{ m}^2 \text{ g}^{-1}$ ). Additionally, the electrical conductivity, which was measured for individual CN macrostructures as previously reported by our group,<sup>18</sup> did not show any clear trend among the materials or any correlation with the structural doping (Scheme S2, Figure S23). Therefore, we concluded that the enhanced photocatalytic activity stems from an improvement in electron–hole pair separation and an enhancement in ionic strength of the media resulting in a dielectric screening effect.

## 4. CONCLUSIONS

In summary, in this work, we have designed alkali metal-containing melamine crystals and utilized them for the high-temperature synthesis of CN materials. The tailored design of the starting crystals allows the incorporation of  $\text{Na}^+$  and  $\text{K}^+$  ions within the bulk of the material and on its surface in their ionic salt form. Consequently, we reveal the synergetic contribution of alkali metals within the CN framework and



in the reaction medium. Detailed experimental characterizations, together with DFT calculations, shed light on the most stable conformation of Na<sup>+</sup> and K<sup>+</sup> within the heptazine lattice. The presence of NaCl and KCl crystals on the surface of the materials enhances the ionic strength of the reaction media in the photocatalysis measurements, promoting the overall activity for the HER and reaching an AQY of 10%. We believe that this work opens the gate toward the one-pot synthesis of C–N materials with tailored surface chemistry and electronic structure for energy-related devices.

## ■ ASSOCIATED CONTENT

### Supporting Information

The Supporting Information is available free of charge at <https://pubs.acs.org/doi/10.1021/acsaem.0c02964>.

Additional crystals and materials characterization using SEM, FTIR, XRD, XPS, TGA, solid-state NMR, optical measurements, and so forth, schemes, electrical measurements, and comparison tables (PDF)

## ■ AUTHOR INFORMATION

### Corresponding Authors

Shmuel Barzilai – Department of Chemistry, Nuclear Research Centre-Negev, Beer-Sheva 84190, Israel;  
✉ [orcid.org/0000-0002-1198-4848](https://orcid.org/0000-0002-1198-4848);  
Email: [barzilai.shmuel@gmail.com](mailto:barzilai.shmuel@gmail.com)

Menny Shalom – Department of Chemistry and Ilse Katz Institute for Nanoscale Science and Technology, Ben-Gurion University of the Negev, Beer-Sheva 8410501, Israel;  
✉ [orcid.org/0000-0002-4506-4177](https://orcid.org/0000-0002-4506-4177); Email: [mennysh@bgu.ac.il](mailto:mennysh@bgu.ac.il)

### Authors

Jesús Barrio – Department of Chemistry and Ilse Katz Institute for Nanoscale Science and Technology, Ben-Gurion University of the Negev, Beer-Sheva 8410501, Israel;  
Department of Materials, Royal School of Mines, Imperial College London<sup>RINGGOLD</sup>, London SW2AZ, England;  
✉ [orcid.org/0000-0002-4147-2667](https://orcid.org/0000-0002-4147-2667)

Neeta Karjule – Department of Chemistry and Ilse Katz Institute for Nanoscale Science and Technology, Ben-Gurion University of the Negev, Beer-Sheva 8410501, Israel

Pilar Amo-Ochoa – Departamento de Química Inorgánica, Institute for Advanced Research in Chemical Sciences, Universidad Autónoma de Madrid, Madrid 28049, Spain;  
✉ [orcid.org/0000-0002-1952-1020](https://orcid.org/0000-0002-1952-1020)

Félix Zamora – Departamento de Química Inorgánica, Institute for Advanced Research in Chemical Sciences and Condensed Matter Physics Institute (IFIMAC), Universidad Autónoma de Madrid, Madrid 28049, Spain; ✉ [orcid.org/0000-0001-7529-5120](https://orcid.org/0000-0001-7529-5120)

Complete contact information is available at:  
<https://pubs.acs.org/doi/10.1021/acsaem.0c02964>

### Author Contributions

The manuscript was written through contributions of all authors. All authors have given approval to the final version of the manuscript.

### Funding

This project has received funding from the European Research Council (ERC) under the European Union's Horizon 2020 research and innovation programme (grant agreement no.

[849068]). It was also partially supported by the Israel Science Foundation (ISF), grant no. 1161/17, and ISF-NSFC grant no. 2969/19. SB acknowledges the Negev HPC project for the support in computational projects. MS and SB thank Pazy Foundation for the support (grant no. 119–2020).

### Notes

The authors declare no competing financial interest.

## ■ ACKNOWLEDGMENTS

We want to thank Adi Azoulay, Liel Abisdri, Jonathan Tzadikov, Dr. Michael Volokh, and Dr. Jiawei Xia for their help with the materials characterization. We also thank the scientific staff at the Ilse Katz Institute for Nanoscale Science and Technology.

## ■ REFERENCES

- (1) Wang, X.; Maeda, K.; Thomas, A.; Takanabe, K.; Xin, G.; Carlsson, J. M.; Domen, K.; Antonietti, M. A Metal-Free Polymeric Photocatalyst for Hydrogen Production from Water under Visible Light. *Nat. Mater.* **2009**, *8*, 76–80.
- (2) Wang, Y.; Vogel, A.; Sachs, M.; Sprick, R. S.; Wilbraham, L.; Moniz, S. J. A.; Godin, R.; Zwiijnenburg, M. A.; Durrant, J. R.; Cooper, A. I.; Tang, J. Current Understanding and Challenges of Solar-Driven Hydrogen Generation Using Polymeric Photocatalysts. *Nat. Energy* **2019**, *4*, 746–760.
- (3) Volokh, M.; Peng, G.; Barrio, J.; Shalom, M. Carbon Nitride Materials for Water Splitting Photoelectrochemical Cells. *Angew. Chem., Int. Ed.* **2019**, *58*, 6138–6151.
- (4) Lin, L.; Lin, Z.; Zhang, J.; Cai, X.; Lin, W.; Yu, Z.; Wang, X. Molecular-Level Insights on the Reactive Facet of Carbon Nitride Single Crystals Photocatalysing Overall Water Splitting. *Nat. Catal.* **2020**, *3*, 649–655.
- (5) Fang, Y.; Wang, X. Photocatalytic CO<sub>2</sub> Conversion by Polymeric Carbon Nitrides. *Chem. Commun.* **2018**, *54*, S674–S687.
- (6) Talapaneni, S. N.; Singh, G.; Kim, I. Y.; AlBahily, K.; Al-Muhtaseb, A. H.; Karakoti, A. S.; Tavakkoli, E.; Vinu, A. Nanostructured Carbon Nitrides for CO<sub>2</sub> Capture and Conversion. *Adv. Mater.* **2020**, *32*, 1904635.
- (7) Barrio, J.; Mateo, D.; Alberro, J.; García, H.; Shalom, M. A Heterogeneous Carbon Nitride–Nickel Photocatalyst for Efficient Low-Temperature CO<sub>2</sub> Methanation. *Adv. Energy Mater.* **2019**, *9*, 1902738.
- (8) Savateev, A.; Ghosh, I.; König, B.; Antonietti, M. Photoredox Catalytic Organic Transformations Using Heterogeneous Carbon Nitrides. *Angew. Chem., Int. Ed.* **2018**, *57*, 15936–15947.
- (9) Xavier, M. M.; Nair, P. R.; Mathew, S. Emerging Trends in Sensors Based on Carbon Nitride Materials. *Analyst* **2019**, *144*, 1475–1491.
- (10) Chen, L.; Song, J. Tailored Graphitic Carbon Nitride Nanostructures: Synthesis, Modification, and Sensing Applications. *Adv. Funct. Mater.* **2017**, *27*, 1702695.
- (11) Xu, J.; Shalom, M. Conjugated Carbon Nitride as an Emerging Luminescent Material: Quantum Dots, Thin Films and Their Applications in Imaging, Sensing, Optoelectronic Devices and Photoelectrochemistry. *ChemPhotoChem* **2019**, *3*, 170–179.
- (12) Cao, Q.; Kumru, B.; Antonietti, M.; Schmidt, B. V. K. J. Graphitic Carbon Nitride and Polymers: A Mutual Combination for Advanced Properties. *Mater. Horiz.* **2020**, *7*, 762–786.
- (13) Kessler, F. K.; Zheng, Y.; Schwarz, D.; Merschjann, C.; Schnick, W.; Wang, X.; Bojdys, M. J. Functional Carbon Nitride Materials—Design Strategies for Electrochemical Devices. *Nat. Rev. Mater.* **2017**, *2*, 17030.
- (14) Safaei, J.; Mohamed, N. A.; Mohamad Noh, M. F.; Soh, M. F.; Ludin, N. A.; Ibrahim, M. A.; Roslam Wan Isahak, W. N.; Mat Teridi, M. A. Graphitic Carbon Nitride (g-C<sub>3</sub>N<sub>4</sub>) Electrodes for Energy Conversion and Storage: A Review on Photoelectrochemical Water

Splitting, Solar Cells and Supercapacitors. *J. Mater. Chem. A* **2018**, *6*, 22346–22380.

(15) Barrio, J.; Volokh, M.; Shalom, M. Polymeric Carbon Nitrides and Related Metal-Free Materials for Energy and Environmental Applications. *J. Mater. Chem. A* **2020**, *8*, 11075–11116.

(16) Jiang, L.; Yuan, X.; Pan, Y.; Liang, J.; Zeng, G.; Wu, Z.; Wang, H. Doping of Graphitic Carbon Nitride for Photocatalysis: A Reveiw. *Appl. Catal., B* **2017**, *217*, 388–406.

(17) Li, X.; Bartlett, S. A.; Hook, J. M.; Sergeyev, I.; Clatworthy, E. B.; Masters, A. F.; Maschmeyer, T. Salt-Enhanced Photocatalytic Hydrogen Production from Water with Carbon Nitride Nanorod Photocatalysts: Cation and PH Dependence. *J. Mater. Chem. A* **2019**, *7*, 18987–18995.

(18) Barrio, J.; Lin, L.; Amo-ochoa, P.; Tzadikov, J.; Peng, G.; Sun, J.; Zamora, F.; Wang, X.; Shalom, M. Unprecedented Centimeter-Long Carbon Nitride Needles: Synthesis, Characterization and Applications. *Small* **2018**, *14*, 1800633.

(19) Zhu, J.-N.; Zhu, X.-Q.; Cheng, F.-F.; Li, P.; Wang, F.; Xiao, Y.-W.; Xiong, W.-W. Preparing Copper Doped Carbon Nitride from Melamine Templated Crystalline Copper Chloride for Fenton-like Catalysis. *Appl. Catal., B* **2019**, *256*, 117830.

(20) Fang, X.; Gao, R.; Yang, Y.; Yan, D. A Cocystal Precursor Strategy for Carbon-Rich Graphitic Carbon Nitride toward High-Efficiency Photocatalytic Overall Water Splitting. *iScience* **2019**, *16*, 22–30.

(21) Azoulay, A.; Barrio, J.; Tzadikov, J.; Volokh, M.; Alberio, J.; Gervais, C.; Amo-Ochoa, P.; Garcia, H.; Zamora, F.; Shalom, M. Synthesis of Metal-Free Lightweight Materials with Sequence-Encoded Properties. *J. Mater. Chem. A* **2020**, *8*, 8752–8760.

(22) Zhang, J.-H.; Wei, M.-J.; Wei, Z.-W.; Pan, M.; Su, C.-Y. Ultrathin Graphitic Carbon Nitride Nanosheets for Photocatalytic Hydrogen Evolution. *ACS Appl. Nano Mater.* **2020**, *3*, 1010–1018.

(23) Jiang, Z.; Zhang, X.; Chen, H. S.; Hu, X.; Yang, P. Formation of G-C 3 N 4 Nanotubes towards Superior Photocatalysis Performance. *ChemCatChem* **2019**, *11*, 4558–4567.

(24) Barrio, J.; Shalom, M. Rational Design of Carbon Nitride Materials by Supramolecular Preorganization of Monomers. *ChemCatChem* **2018**, *10*, 5573–5586.

(25) Barrio, J.; Shalom, M. Ultralong Nanostructured Carbon Nitride Wires and Self-Standing C-Rich Filters from Supramolecular Microspheres. *ACS Appl. Mater. Interfaces* **2018**, *10*, 39688–39694.

(26) Kalisman, P.; Nakibli, Y.; Amirav, L. Perfect Photon-to-Hydrogen Conversion Efficiency. *Nano Lett.* **2016**, *16*, 1776–1781.

(27) Giannozzi, P.; Baroni, S.; Bonini, N.; Calandra, M.; Car, R.; Cavazzoni, C.; Ceresoli, D.; Chiarotti, G. L.; Cococcioni, M.; Dabo, I.; Dal Corso, A.; de Gironcoli, S.; Fabris, S.; Fratesi, G.; Gebauer, R.; Gerstmann, U.; Gougoussis, C.; Kokalj, A.; Lazzeri, M.; Martin-Samos, L.; Marzari, N.; Mauri, F.; Mazzarello, R.; Paolini, S.; Pasquarello, A.; Paulatto, L.; Sbraccia, C.; Scandolo, S.; Sclauzero, G.; Seitsonen, A. P.; Smogunov, A.; Umari, P.; Wentzcovitch, R. M. QUANTUM ESPRESSO: A Modular and Open-Source Software Project for Quantum Simulations of Materials. *J. Phys.: Condens. Matter* **2009**, *21*, 395502.

(28) Desclaux, J. P. Hartree Fock Slater Self Consistent Field Calculations. *Comput. Phys. Commun.* **1970**, *1*, 216–222.

(29) Perdew, J. P.; Burke, K.; Ernzerhof, M. Generalized Gradient Approximation Made Simple. *Phys. Rev. Lett.* **1996**, *77*, 3865.

(30) Monkhorst, H. J.; Pack, J. D. Special Points for Brillouin-Zone Integrations. *Phys. Rev. B: Solid State* **1976**, *13*, 5188.

(31) Athikomrattanakul, U.; Promptmas, C.; Katterle, M.; Schilde, U. An Ortho{\-}rhombic Polymorph of Melaminium Chloride Hemihydrate. *Acta Crystallogr., Sect. E: Crystallogr. Commun.* **2007**, *63*, o2154–o2156.

(32) Janczak, J.; Perpétuo, G. J. Melaminium Chloride Hemihydrate. *Acta Crystallogr., Sect. C: Struct. Chem.* **2001**, *57*, 1120–1122.

(33) Weng, D.-F.; Wang, B.-W.; Wang, Z.-M.; Gao, S.; H2mela. 2[FeCl5]Cl (Mela = Melamine): A Cl-Bridged Single-Chain Magnet Based on Weak Ferromagnetism. *Coord. Chem. Rev.* **2013**, *257*, 2484–2490.

(34) Weng, D.-F.; Wang, B.-W.; Wang, Z.-M.; Gao, S. Polymorphism of (H2mela)2[CuCl5]Cl (Mela = Melamine): Structures, Transformation and Magnetic Properties. *CrystEngComm* **2011**, *13*, 4683–4688.

(35) Priya, M.; Mahadevan, C. K. Preparation and Dielectric Properties of Oxide Added NaCl–KCl Polycrystals. *Phys. Rev. B: Condens. Matter Mater. Phys.* **2008**, *403*, 67–74.

(36) Li, H.-L.; Du, Z.-N.; Wang, G.-L.; Zhang, Y.-C. Low Temperature Molten Salt Synthesis of SrTiO3 Submicron Crystallites and Nanocrystals in the Eutectic NaCl–KCl. *Mater. Lett.* **2010**, *64*, 431–434.

(37) Janczak, J.; Perpétuo, G. J. Melaminium Chloride Hemihydrate. *Acta Crystallogr., Sect. C: Struct. Chem.* **2001**, *57*, 1120–1122.

(38) Wang, W.; Zhang, H.; Zhang, S.; Liu, Y.; Wang, G.; Sun, C.; Zhao, H. Potassium-Ion-Assisted Regeneration of Active Cyano Groups in Carbon Nitride Nanoribbons: Visible-Light-Driven Photocatalytic Nitrogen Reduction. *Angew. Chem., Int. Ed.* **2019**, *58*, 16644–16650.

(39) Zhang, M.; Bai, X.; Liu, D.; Wang, J.; Zhu, Y. Enhanced Catalytic Activity of Potassium-Doped Graphitic Carbon Nitride Induced by Lower Valence Position. *Appl. Catal., B* **2015**, *164*, 77–81.

(40) Zhang, J.; Hu, S.; Wang, Y. A Convenient Method to Prepare a Novel Alkali Metal Sodium Doped Carbon Nitride Photocatalyst with a Tunable Band Structure. *RSC Adv.* **2014**, *4*, 62912–62919.

(41) Ding, Z.; Chen, X.; Antonietti, M.; Wang, X. Synthesis of Transition Metal-Modified Carbon Nitride Polymers for Selective Hydrocarbon Oxidation. *ChemSusChem* **2011**, *4*, 274–281.

(42) Zhang, Q.; Chen, P.; Tan, C.; Chen, T.; Zhuo, M.; Xie, Z.; Wang, F.; Liu, H.; Cai, Z.; Liu, G.; Lv, W. A Photocatalytic Degradation Strategy of PPCPs by a Heptazine-Based CN Organic Polymer (OCN) under Visible Light. *Environ. Sci.: Nano* **2018**, *5*, 2325–2336.

(43) Jürgens, B.; Irran, E.; Senker, J.; Kroll, P.; Müller, H.; Schnick, W. Melem (2,5,8-Triamino-Tri-s-Triazine), an Important Intermediate during Condensation of Melamine Rings to Graphitic Carbon Nitride: Synthesis, Structure Determination by X-Ray Powder Diffractometry, Solid-State NMR, and Theoretical Studies. *J. Am. Chem. Soc.* **2003**, *125*, 10288–10300.

(44) Ran, J.; Zhang, H.; Qu, J.; Shan, J.; Chen, S.; Yang, F.; Zheng, R.; Cairney, J.; Song, L.; Jing, L.; Qiao, S.-Z. Atomic-Level Insights into the Edge Active ReS2 Ultrathin Nanosheets for High-Efficiency Light-to-Hydrogen Conversion. *ACS Mater. Lett.* **2020**, *2*, 1484–1494.

(45) Ran, J.; Qu, J.; Zhang, H.; Wen, T.; Wang, H.; Chen, S.; Song, L.; Zhang, X.; Jing, L.; Zheng, R.; Qiao, S. Z. 2D Metal Organic Framework Nanosheet: A Universal Platform Promoting Highly Efficient Visible-Light-Induced Hydrogen Production. *Adv. Energy Mater.* **2019**, *9*, 1803402.